PCCP

PAPER

View Article Online
View Journal | View Issue

Cite this: *Phys. Chem. Chem. Phys.*, 2016, **18**, 24746

Photoionization-induced π ↔ H site switching dynamics in phenol$^+$–Rg (Rg = Ar, Kr) dimers probed by picosecond time-resolved infrared spectroscopy†

Mitsuhiko Miyazaki,[a] Yuri Sakata,[a] Markus Schütz,[b] Otto Dopfer*[b] and Masaaki Fujii*[a]

Received 20th July 2016,
Accepted 14th August 2016

DOI: 10.1039/c6cp05016f

www.rsc.org/pccp

The ionization-induced π ↔ H site switching reaction in phenol$^+$–Rg (PhOH$^+$–Rg) dimers with Rg = Ar and Kr is traced in real time by picosecond time-resolved infrared (ps-TRIR) spectroscopy. The ps-TRIR spectra show the prompt appearance of the non-vanishing free OH stretching band upon resonant photoionization of the π-bound neutral clusters, and the delayed appearance of the hydrogen-bonded (H-bonded) OH stretching band. This result directly proves that the Rg ligand switches from the π-bound site on the aromatic ring to the H-bonded site at the OH group by ionization. The subsequent H → π back reaction converges the dimer to a π ↔ H equilibrium. This result is in sharp contrast to the single-step π → H forward reaction in the PhOH$^+$–Ar$_2$ trimer with 100% yield. The reaction mechanism and yield strongly depend on intracluster vibrational energy redistribution. A classical rate equation analysis for the time evolutions of the band intensities of the two vibrations results in similar estimates for the time constants of the π → H forward reaction of τ_+ = 122 and 73 ps and the H → π back reaction of τ_- = 155 and 188 ps for PhOH$^+$–Ar and PhOH$^+$–Kr, respectively. The one order of magnitude slower time constant in comparison to the PhOH$^+$–Ar$_2$ trimer (τ_+ = 7 ps) is attributed to the decrease in density of states due to the absence of the second Ar in the dimer. The similar time constants for both PhOH$^+$–Rg dimers are well rationalized by a classical interpretation based on the comparable potential energy surfaces, reaction pathways, and density of states arising from their similar intermolecular vibrational frequencies.

1. Introduction

Nonpolar solvents like rare gas (Rg) atoms and CH_4 solvating phenol (PhOH) or related molecules change the most stable binding site upon ionization of the PhOH solute (site switching) from the dispersive aromatic π-cloud to the hydrogen bonding OH group.[1–3] The dynamics of this intermolecular π → H (hydrophobic → hydrophilic) site switching reaction triggered by ionization has been measured in real time by applying picosecond time-resolved vibrational (infrared) spectroscopy (ps-TRIR) to molecular clusters isolated in the gas phase.[1,2,4–7] This π → H switching reaction enables us to investigate fundamental aspects of solvation dynamics induced by photoexcitation in a well-defined molecular system. Solvation dynamics is the initial step in solution-phase chemistry, and aromatic molecules such as phenol play a fundamental role in biological and chemical recognition processes.[8–16] They significantly affect the energetics and dynamics of chemical reactions and structural rearrangements, for example protein folding and the self-assembly of supramolecules and nanostructures.[17–19] In this context, PhOH–S$_n$ clusters with nonpolar solvent atoms or molecules (S = Rg, CH_4) serve as a benchmark system not only for experimental works[1–7,20–41] but also for accurate quantum chemical calculations.[26,40,42–44]

In the neutral ground electronic states (S_0) of PhOH–S$_n$ dimers (n = 1), these nonpolar solvents bind to the π electron cloud of PhOH mainly by dispersion forces,[20–22,35] and the OH binding site is at most a shallow local minimum.[40,42–44] When multiple Rg atoms solvate the π-cloud, the way of condensation of the Rg atoms in PhOH–Rg$_n$ ($n \geq 2$) is determined by the relative strengths of the Rg–Rg and π–Rg interactions. In PhOH–Rg$_n$ clusters, the coexistence of both types of condensation (single-sided and double-sided) has been established by

[a] *Laboratory for Chemistry and Life Science, Institute of Innovative Research, Tokyo Institute of Technology, Yokohama 226-8503, Japan. E-mail: mfujii@res.titech.ac.jp*
[b] *Institut für Optik und Atomare Physik, Technische Universität Berlin, 10623 Berlin, Germany. E-mail: dopfer@physik.tu-berlin.de*

† Electronic supplementary information (ESI) available. See DOI: 10.1039/c6cp05016f

the analysis of characteristic shifts of the electronic S_1–S_0 transition.[7,40]

Deposition of a positive charge on PhOH switches the dominant intermolecular interaction site from the π electron system to the OH group, due to the additional charge-induced polarization forces, which substantially enhance the strength of hydrogen bonding.[3,28–30,34,37,39,40,45] Thus, one of the nonpolar solvent moieties moves to the OH group, when the cluster is ionized into the ground electronic state of the cation (D_0). The mechanism and time scale of this process have been investigated in PhOH–Rg_n clusters by ps-TRIR spectroscopy and both are found to depend on the degree of solvation (n).[1,2,4–7]

In the larger $PhOH^+$–Rg_n clusters ($n \geq 2$), the reaction proceeds in a one-way, single step π → H forward reaction with 100% yield.[4,5,7] The excess energy released by the exothermic reaction is removed from the reaction coordinate and redistributed to low frequency vibrational bath modes by intracluster vibrational energy redistribution (IVR), which are composed mainly of intermolecular vibrations of the Rg atoms that remain at the π-cloud.[5,7,45] As a result, the H → π back reaction is efficiently quenched, leading to essentially 100% yield for the π → H forward reaction.

The reaction mechanism of a $PhOH^+$–Rg dimer (n = 1) with an atomic ligand is qualitatively different from that in $PhOH^+$–Rg_n ($n \geq 2$).[6,41] In the dimer, there are only three intermolecular degrees of freedom arising from the three translational motions of Rg, and the isomerization coordinate from the out-of-plane π-cloud to the in-plane OH group must be constructed from all three translational degrees of freedom. In addition, the lowest frequency intramolecular vibration of $PhOH^+$ is 177 cm^{-1},[46] *i.e.* much larger than the low-frequency intermolecular vibrations of the $PhOH^+$–Rg dimer. Thus, the excess energy is distributed predominantly among the intermolecular modes. This means that the excess energy remains always in the reaction coordinate, *i.e.* there are no available bath modes to accept the excess energy. Therefore, the Rg atom cannot stay in the OH global minimum and it undergoes a H → π back reaction toward the two degenerate π-bound local minima below and above the aromatic ring (Fig. 1). Therefore, the isomerization reaction reaches a π ↔ H equilibrium population of the π-bound and OH-bound structures in the case of the n = 1 dimer, leading to a finite reaction yield well below 100%. This behavior is different for (acidic) aromatic dimers with polyatomic solvent molecules (S = H_2O, CH_4),[1,2,45,47–51] because then even in the dimers (n = 1) bath modes are available for IVR, which quench the back reaction.

So far, the real time dynamics of the π ↔ H equilibrium has been observed only for the $PhOH^+$–Kr (n = 1) dimer.[6] Although π → H reactions in $PhOH^+$–Ar_n (n = 2 and 3) have been studied,[4,5,7] there is no report on the dynamics of the $PhOH^+$–Ar dimer. Though the similarity of static IR spectroscopy of the $PhOH^+$–Ar and $PhOH^+$–Kr dimers suggests that the dynamics for Rg = Ar is also analogous to Rg = Kr, comparison of the dynamics in larger clusters for the same solvent species (here Ar) is indispensable for the systematic study of the size dependence of the dynamics. In addition, as for the mechanism

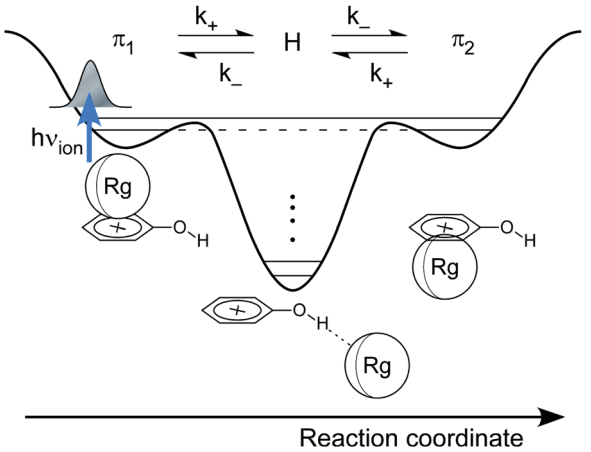

Fig. 1 Sketch of the potential energy diagram of $PhOH^+$–Rg dimers in the cationic D_0 state along the reaction coordinate for the ionization-induced π ↔ H site switching. The H-bound structure (H) is the global minimum of the potential, while the two π-bound structures (π_1 and π_2), in which Rg is located on either side of the aromatic ring, are local minima. The rate constants for the forward and backward reactions used in the simple classical pendular model are indicated. Calculated binding energies for minima and barriers are available in Table 1.

of the site switching of $PhOH^+$–Ar, a significant contribution of direct ionization from the π-bound to the OH-bound structure and the existence of a tiny activation barrier for the π → H isomerization have been reported from IR spectroscopy on the cationic D_0 state and high-n Rydberg states.[41] Ionization of the clusters above the barrier initially generates a wavepacket localized at the π-bound site. This wavepacket then propagates to the H-bound site, and finally spreads over the whole region between the π and OH sites due to dephasing.[6] To clarify this dynamics, a real-time observation using picosecond lasers has to be carried out. The present study aims to measure the isomerization process of $PhOH^+$–Ar, and the dynamics of $PhOH^+$–Kr is revisited under the same, improved experimental conditions to directly compare the dynamics of the two Rg atoms by ps-TRIR spectroscopy.

2. Experimental and computational details

Details of the picosecond time-resolved UV–UV–IR ion dip spectroscopy and the employed experimental setup have been described elsewhere.[1,2,4] Briefly, PhOH–Rg clusters are produced in a supersonic jet by expanding phenol vapor at room temperature seeded in mixtures of 10% Ar or 1% Kr in He at 2–3 bars stagnation pressure through a pulsed valve into a vacuum chamber. The clusters pass through a skimmer into the ionization region of a time-of-flight (TOF) mass spectrometer. The PhOH–Rg dimers are resonantly ionized *via* the first singlet excited state (S_1) using two picosecond UV laser pulses. The wavelength of the first UV laser, ν_{exc}, is tuned to the S_1 origin band of each cluster. The second UV laser, ν_{ion}, ionizes the excited cluster with little excess energy into the cation ground state (D_0). The delay time between ν_{exc}

and ν_{ion} is set to 100–250 ps. The ions generated are extracted into the TOF mass spectrometer and detected. While monitoring the mass-selected $PhOH^+$–Rg ion current, a tunable picosecond IR laser, ν_{IR}, is fired and scanned in the OH stretching range with an adjustable delay (Δt) with respect to ν_{ion}. The ion signal is amplified, integrated, and monitored as a function of ν_{IR} and/or Δt. If ν_{IR} is resonant with a vibrational transition of $PhOH^+$–Rg, the cluster dissociates upon vibrational excitation, leading to a depletion of the monitored parent ion current. Thus, the IR spectrum of $PhOH^+$–Rg is obtained by monitoring the depletion of its ion current as a function of ν_{IR}. The depletion is converted to absorbance by taking the logarithm of the depletion. All the laser beams are combined coaxially and focused by a CaF_2 lens with f = 275 mm focal length into the supersonic jet. The intensity of the ν_{IR} beam is carefully adjusted not to saturate the IR depletion by controlling its focal point using a telescope. The energies of the UV and IR pulses are less than 10 and 30 μJ, respectively. The energy and time resolution of the picosecond laser pulses are $\sim$12 cm^{-1} and $\sim$3 ps, respectively. Similar spectroscopic experiments are carried out using standard nanosecond laser systems.

Dispersion-corrected density functional theory calculations are employed to determine the salient parts of the $PhOH^+$–Rg potential energy surface in the D_0 state, with a particular focus on the properties of the stationary points.[52] To this end, structural, vibrational, and energetic properties of the H-bound and π-bound minima and their connecting transition states are evaluated at the B3LYP-D3/aug-cc-pVTZ level (Table 1). This level reliably describes the interaction of the Rg atoms with the $PhOH^+$ cation in its doublet ground electronic state, as shown by the good agreement between the experimental and computational binding energies of the π-bound and H-bound $PhOH^+$–Ar cation (Table 1). Spin contamination is negligible at this theoretical level, with values of $\langle S^2\rangle - 0.75 < 0.0001$ and 0.015 after and before spin annihilation, respectively. All interaction energies (D_e) are corrected for harmonic vibrational zero-point energies to derive binding energies (D_0). Harmonic intramolecular vibrational frequencies are scaled by a factor of 0.9554 to match the calculated with the experimental OH stretching frequency of bare $PhOH^+$ (ν_{OH} = 3534 cm^{-1}).[53] Reported intermolecular frequencies (ν_s, ν_{b1}, ν_{b2}) remain unscaled.

3. Results and discussion

3.1 Computational results

Table 1 collects the computational results for $PhOH^+$ and $PhOH^+$–Rg relevant for the present work, along with available experimental data. In general, the interaction in $PhOH^+$–Kr is roughly 30–35% stronger than in $PhOH^+$–Ar due to the larger polarizability of the Rg atom (α = 2.465 *versus* 1.63 $Å^3$). For both Rg atoms, the H-bonded structure is the global minimum on the potential (Fig. 1), with binding energies of D_0 = 1271 and 952 cm^{-1} and bond lengths of $R_{OH\cdots Rg}$ = 2.50 and 2.39 Å, respectively. H-bonding results in an elongation of the OH bond by Δr_{OH} = 5.2 and 3.2 mÅ for Rg = Kr and Ar, and corresponding frequency red shifts of $-\Delta\nu_{OH}^{H}$ = 118 and 74 cm^{-1}, which are in excellent agreement with the measured values of 123 and 70 cm^{-1}, respectively.[30,34] H-bonding increases the IR activity of ν_{OH}^{H} (I_{OH}) by factors of 3.35 (Kr) and 2.62 (Ar). The less stable π-bonded local minima of $PhOH^+$–Rg have dissociation energies of D_0 = 777 and 548 cm^{-1} and bond distances of $R_{\pi\cdots Rg}$ = 3.67 and 3.54 Å for Kr and Ar, respectively. As expected, π-bonded ligands have almost no impact on the OH bond length ($\Delta r_{OH} < 0.3$ mÅ), stretching frequency ($\Delta\nu_{OH}^{H} < 3$ cm^{-1}), and IR activity ($\Delta I_{OH} < 7\%$) of $PhOH^+$. Interestingly, the frequencies of the intermolecular stretching (ν_s) and the two bending modes (ν_{b1}, ν_{b2}) are quite similar for both isomers of $PhOH^+$–Rg for both Rg = Ar and Kr (Table 1), with good agreement with experimental frequencies for the π-bonded structures available from high-resolution photoelectron spectroscopy.[27,31] The similar intermolecular frequencies imply comparable vibrational density of states for both $PhOH^+$–Rg dimers. Significantly, the dissociation energies calculated for $PhOH^+$–Ar(π) and $PhOH^+$–Ar(H), D_0 = 548 and 952 cm^{-1}, are in excellent agreement with the measured values of 535 ± 3 and 905 cm^{-1},[25,37] confirming that the employed B3LYP-D3/aug-cc-pVTZ level provides a reliable

Table 1 Structural, vibrational, and energetic parameters of $PhOH^+$ and $PhOH^+$–Rg dimers in the cation ground state (D_0) evaluated at the B3LYP-D3/aug-cc-pVTZ level, along with available experimental data (in italics)

	$PhOH^+$	$PhOH^+$–Ar(H)	$PhOH^+$–Ar(π)	$PhOH^+$–Kr(H)	$PhOH^+$–Kr(π)
r_{OH} [Å]	0.97165	0.97488	0.97145	0.97680	0.97136
ν_{OH} [a] [cm^{-1}]	3534	3460	3536	3416	3537
ν_{OH} [b] [cm^{-1}] exp	*3534*	*3464*	*3536*	*3411*	*3535*
I_{OH} [km mol^{-1}]	265	694	255	889	248
D_e [cm^{-1}]	—	1027	642	1336	863
D_0 [cm^{-1}]	—	952	548	1271	777
D_0 [c] [cm^{-1}] exp	—	*905*	*535 ± 3*	—	—
$V_{b\pm}$ [cm^{-1}]		413	28	516	43
$R_{OH\cdots Rg}$ [Å]	—	2.393	—	2.499	—
$R_{C1\cdots Rg}$ [Å]	—	—	3.410	—	3.501
$R_{\pi\cdots Rg}$ [d] [Å]	—	—	3.535	—	3.668
ν_s [e] [cm^{-1}]	—	70	60 (*66*)	59	55 (*64*)
ν_{b1} [e] [cm^{-1}]	—	30	34 (*25*)	33	37 (*29*)
ν_{b2} [e] [cm^{-1}]	—	30	25 (*15*)	29	22 (*17*)

[a] Scaled by a factor of 0.9554 to match the experimental and calculated frequencies of $PhOH^+$. [b] Ref. 30, 34 and 53. [c] Ref. 25 and 37. [d] Measured from the center of the aromatic ring. [e] Experimental values from ref. 27 and 31.

description of both the π-stacking and H-bonding regions of the $PhOH^+$–Rg potentials. In general, the topology of the $PhOH^+$–Rg potential is quite similar for Rg = Ar and Kr. In particular, the structural parameters of the $PhOH^+$–Rg minima are almost the same for Rg = Ar and Kr (Table 1), suggesting that the π ↔ H isomerization paths are comparable in both direction and length for the two Rg atoms. The calculated barriers for the π → H forward and H → π backward reaction are V_{b+} = 28 and 43 cm^{-1} and V_{b-} = 413 and 516 cm^{-1} for Rg = Ar and Kr, respectively (Fig. S1 in ESI†). Thus, the major difference between the two potentials is merely the stronger interaction in $PhOH^+$–Kr.

3.2 REMPI and PIE spectra

Fig. 2(a) and (b) show 1 + 1′ REMPI spectra of PhOH–Ar and PhOH–Kr, respectively. The blue and red traces in each panel correspond to spectra measured by use of nanosecond and picosecond lasers, respectively. The strongest band in each spectrum is assigned to the S_1 origin band (36 349 and 36 296 cm^{-1})[21,22,54] of the clusters. The nanosecond spectra well reproduce those in previous reports.[21,31] The S_1 origin bands are well isolated and ensure a selective probe of the n = 1 dimers even in the broader picosecond spectra. The wavelength of ν_{exc} is tuned to the S_1 origin bands for the time resolved experiments. The black traces present the REMPI spectrum of the PhOH monomer recorded simultaneously with the dimer spectra. They confirm the soft ionization condition of the clusters because of the lack of fragmentation.

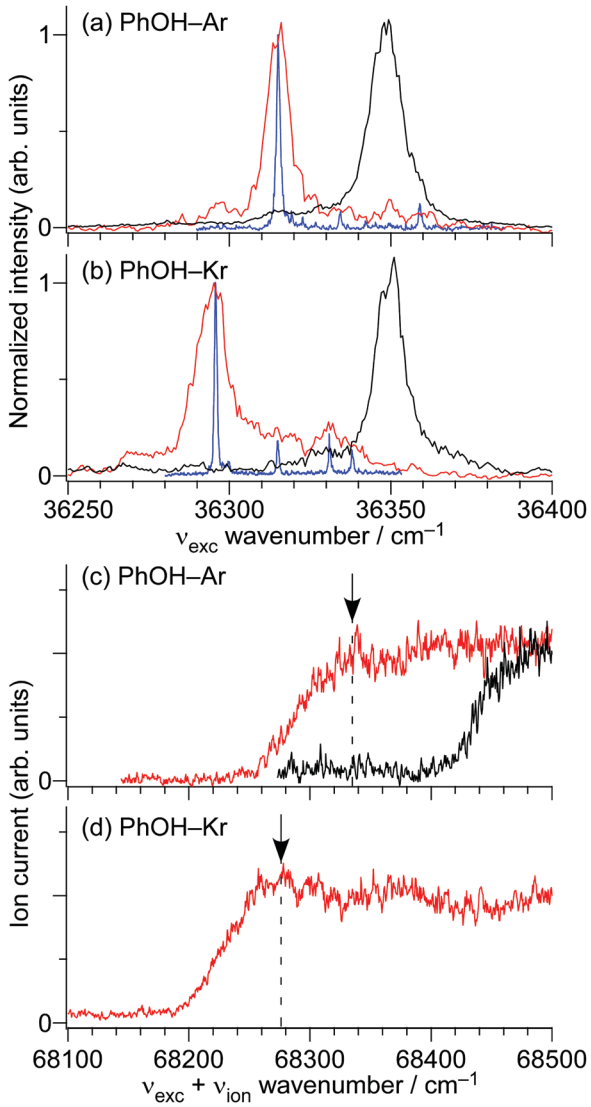

Fig. 2 1 + 1′ REMPI and PIE spectra of PhOH–Ar (a and c) and PhOH–Kr (b and d) recorded by nanosecond (blue) and picosecond (red) lasers. The REMPI and PIE spectra of the PhOH monomer recorded by picosecond lasers (black) are also shown. The ionization excess energies used for the ps-TRIR experiments are indicated by arrows.

Fig. 2(c) and (d) display photoionization efficiency (PIE) spectra of PhOH–Ar and PhOH–Kr, respectively, recorded by picosecond lasers *via* their S_1 origins. The PIE curves rise at ~200 cm^{-1} below the adiabatic ionization energies (IE_0) of each cluster (68 452 and 68 394 cm^{-1} for PhOH–Ar and PhOH–Kr, respectively)[25,27,31] due to the high DC extraction field (~1 kV cm^{-1}) applied in the ionization region of the TOF mass spectrometer. In the ps-TRIR experiments, the ν_{ion} frequency is set to ~80 cm^{-1} above the red-shifted ionization energies of PhOH–Ar and PhOH–Kr, respectively, as indicated by arrows in Fig. 2(c) and (d).

3.3 ps-TRIR spectra

Fig. 3(a) and (b) show the ps-TRIR spectra recorded for $PhOH^+$–Ar and $PhOH^+$–Kr, respectively. The blue spectra at the bottom of each panel reproduce static IR spectra in the D_0 state measured by nanosecond lasers, for which the ionization energies are set to ~80 cm^{-1} above IE_0 for Rg = Ar and Kr, respectively, *i.e.*, well above the barriers calculated as V_{b+} = 28 and 43 cm^{-1}. These spectra correspond to the final products of the solvent rearrangement reactions. When ν_{IR} is introduced before the ionization event ($\Delta t < 0$), no absorption is detected in the ps-TRIR spectra, because the ν_{OH} bands of the neutral dimers occur outside of the scanning range (>3600 cm^{-1}).[2,5] After the ionization, a strong band appears at 3537 cm^{-1} that matches with ν_{OH}^{π} of the π-bound $PhOH^+$–Rg structures in the D_0 state.[22,39] This observation is consistent with the fact that the π-bound neutral clusters are selectively ionized by the 1 + 1′ REMPI process. Although the ν_{OH}^{π} band of the D_0 state remains visible for all delay times (up to 50 ns), a second weak band gradually grows in intensity at 3490 and 3460 cm^{-1} for Rg = Ar and Kr, respectively, that well matches with ν_{OH}^{H} of the corresponding H-bound $PhOH^+$–Rg structures in the D_0 state.[34,39] The ν_{OH}^{H} absorption has reached an almost constant level around 50 ps after the ionization, and the ps-TRIR spectra at around 125 ps closely resemble the static ones recorded in the D_0 state at 50 ns delay. The band width is broader in the picosecond spectra due to the lower spectral resolution of the employed lasers. This broadening is particularly apparent for the sharper ν_{OH}^{π} band. The delayed appearance of the ν_{OH}^{H} band after the ionization event directly proves that the H-bound structure is produced by π → H isomerization from the initially prepared π-bound cation structure. The final intensity of ν_{OH}^{H} is weak compared to that of ν_{OH}^{π}. These intensity ratios reflect the final

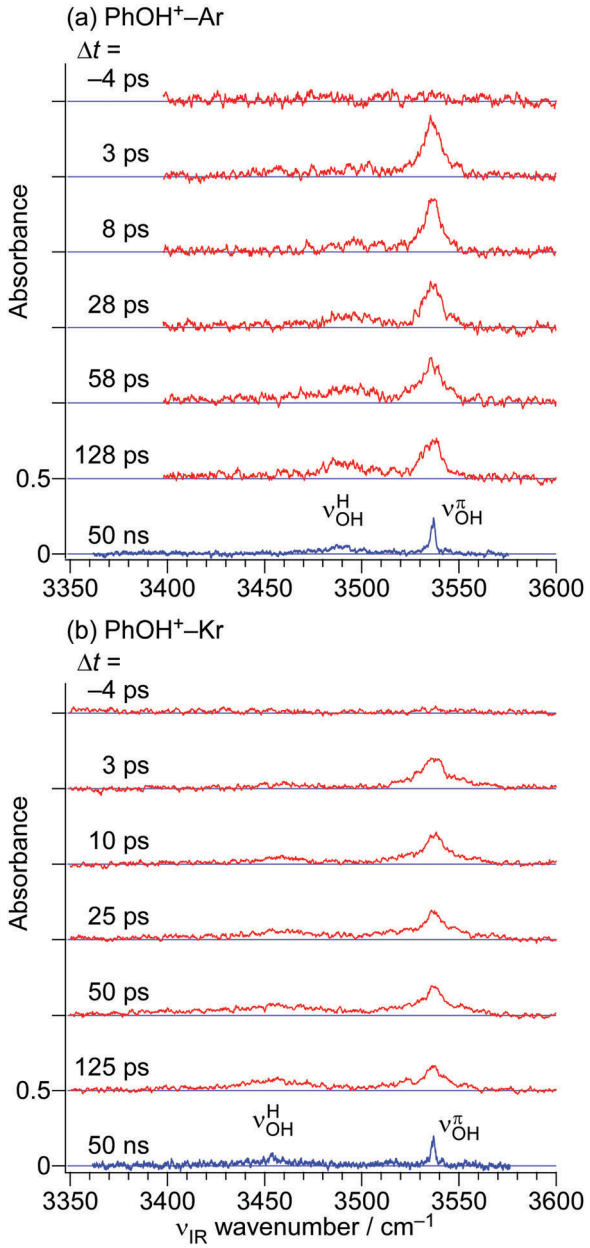

Fig. 3 ps-TRIR spectra (red) of (a) $PhOH^+$–Ar and (b) $PhOH^+$–Kr for variable delay times (Δt). Blue traces at the bottom of the panels show static IR spectra in the cationic state recorded by nanosecond lasers at Δt = 50 ns. The assignments of the bands are indicated in the figures.

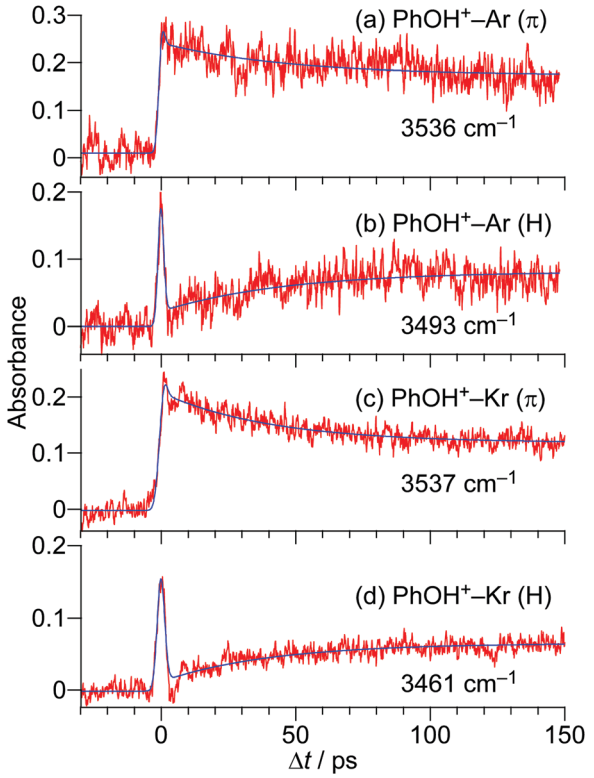

Fig. 4 Time evolution of the ν_{OH}^{π} and ν_{OH}^{H} bands of $PhOH^+$–Ar (a and b) and $PhOH^+$–Kr (c and d) recorded at the frequencies indicated in each panel (see Fig. 3). The blue curves represent the best fit obtained by the three-state reaction model described in the text (Fig. 1). In the time evolution of the ν_{OH}^{H} bands, the peak near Δt = 0 is due to a coherent spike and not related to formation of the H-bound cluster. The profile of the spike corresponds to the cross-correlation function between the UV and IR laser pulses and confirms the overall time resolution of 3 ps. This effect is included in the fitting procedure.

population distribution of H-bound and π-bound structures related to the reaction yield. Although the H-bound structure is the global minimum in D_0,[28–30,40,42,43] the reaction yield is limited and far below unity. This strongly reduced reactivity has been attributed to ineffective IVR in the cationic clusters.[6,41,45] The reaction yield will be discussed in Section 3.4 along with the time evolution of the ν_{OH}^{π} and ν_{OH}^{H} bands.

3.4 Time evolution of vibrational bands

Fig. 4 shows the time evolutions of the ν_{OH}^{π} and ν_{OH}^{H} bands of $PhOH^+$–Ar and $PhOH^+$–Kr, respectively. The absorption of ν_{OH}^{π} rises simultaneously with the ionization at Δt = 0 and subsequently decays to a constant level. The ν_{OH}^{H} band, on the other hand, grows slowly with the delay time, and converges at around Δt = ~100 ps after the ionization also to a constant level. The short enhancement of the ν_{OH}^{H} absorption at Δt = 0 is due to a coherent overlap between the ν_{ion} and ν_{IR} pulses. Thus, the width of this coherent spike reflects the cross correlation of the two pulses, which corresponds to the instrumental time resolution (~3 ps). Though the shape of the time evolutions of both species resemble each other, $PhOH^+$–Kr exhibits a larger drop of the ν_{OH}^{π} band at long delay. This result means that a larger amount of the initially prepared the π-bound structure is eventually converted into the H-bound structure.

To deduce the reaction rate, the time evolutions are fitted on the basis of a slightly modified pendular model proposed previously.[6,41] In this model, the equilibrium between the single H-bound structure and the two equivalent π-bound structures above and below the aromatic ring are considered, $\pi_1 \rightleftharpoons H \rightleftharpoons \pi_2$ (Fig. 1). Resonant photoionization from the S_1 state prepares a wavepacket in one of the π-bound sites of the D_0 state. This wavepacket propagates toward the H-bound global minimum with kinetic energy given by the Franck–Condon

factors for the ionization step. The isomerization does not stop at the H-bound minimum because the excess energy from the exothermic π → H reaction cannot be dissipated from the reaction coordinate into bath modes by IVR in the $PhOH^+$–Rg dimers, and the wavepacket continues to move toward the other π-bound site and/or back to original π-bound site. Finally, the wavepacket spreads out over the whole energetically accessible potential region and converges to an equilibrium by dephasing processes. Such a reaction can be simulated in the simplest way by a basic three-state model with classical rate equations as follows:

$$\frac{d[\pi_1]}{dt} = -k_+([\pi_1] - \alpha) + k_-([H] - \beta) \quad (1)$$

$$\frac{d[H]}{dt} = k_+([\pi_1] - \alpha) - 2k_-([H] - \beta) + k_+[\pi_2] \quad (2)$$

$$\frac{d[\pi_2]}{dt} = -k_+[\pi_2] + k_-([H] - \beta). \quad (3)$$

Here, [X] denotes the concentration of the state X, and α and β represent the population of nonreactive vibrational states of the π-bound and H-bound isomers lying below the isomerization barriers, respectively.[41] These components cannot isomerize and thus contribute as constants to the populations. The factor 2 for k_- in eqn (2) arises from the two degenerate paths to escape from the H-bound structure to the two equivalent π-sites. These equations are further simplified to a two-state model by considering only the summed population of both π-sites because we cannot distinguish them:

$$\frac{d[\pi_1 + \pi_2]}{dt} = -k_+([\pi_1 + \pi_2] - \alpha) + 2k_-([H] - \beta) \quad (1')$$

$$\frac{d[H]}{dt} = k_+([\pi_1 + \pi_2] - \alpha) - 2k_-([H] - \beta). \quad (2')$$

The solution of the eqn (1′) and (2′), under the initial condition of $[\pi_1 + \pi_2](t = 0) = 1 - \beta$ and $[H](t = 0) = \beta$ is

$$[\pi_1+\pi_2] = (1 - \alpha - \beta)\left(\frac{k_+}{k_+ + 2k_-}e^{-(k_+ + 2k_-)t} + \frac{2k_-}{k_+ + 2k_-}\right) + \alpha \quad (4)$$

$$[H] = (1 - \alpha - \beta)\frac{k_+}{k_+ + 2k_-}\left(1 - e^{-(k_+ + 2k_-)t}\right) + \beta. \quad (5)$$

Here, we assume that both $PhOH^+$–Ar and $PhOH^+$–Kr follow the same reaction scheme based on the similar structure of the interaction potential curves, though exact reactivities of $PhOH^+$–Kr from single vibrational levels have not been reported yet. The PIE curves in Fig. S2 (ESI†) provide an estimate of $\alpha = 0.22$ and $\beta = 0.10$ (with error of ±0.02) for both Rg = Ar and Kr. The weak absorption at ν_{OH}^{H} at Δt = 3 ps in Fig. 3 may originate from such direct ionization processes. In the global fit of the measured time evolutions to eqn (4) and (5) the convolution of the instrumental response function is taken into account. The contribution from the coherent spikes are included in the fit by a Gaussian function at Δt = 0. The obtained reaction time constants are $\tau_+ = 122 \pm 18$ ps and $\tau_- = 155 \pm 24$ ps for $PhOH^+$–Ar, and $\tau_+ = 73 \pm 4$ ps and $\tau_- = 188 \pm 12$ ps for $PhOH^+$–Kr. The best fits are included as blue traces in Fig. 4. The results well reproduce the experimental time evolutions. The forward reaction is significantly faster than the backward one in $PhOH^+$–Kr. This is consistent with the observed larger intensity drop in ν_{OH}^{π} of $PhOH^+$–Kr. The difference in the time constants is related to the reaction yield given by the population at long delay through the equation:

$$\frac{[H]}{[\pi_1+\pi_2]}(t \to \infty) = \frac{(1 - \alpha - \beta)k_+ + \beta(k_+ + 2k_-)}{(1 - \alpha - \beta)2k_- + \alpha(k_+ + 2k_-)} = \frac{(1 - \alpha - \beta)\tau_- + \beta(\tau_- + 2\tau_+)}{(1 - \alpha - \beta)2\tau_+ + \alpha(\tau_- + 2\tau_+)}. \quad (6)$$

From this relation and the obtained time constants, the final population ratio of the H-bound and π-bound structures is estimated to be 0.59 (±0.12) for $PhOH^+$–Ar and 0.94 (±0.07) for $PhOH^+$–Kr. The final equilibrium population ratio can also be estimated from relative integrated intensities in the static IR spectra in the cationic D_0 states shown in Fig. 3. The integration of the spectra after converting the depletion to absorbance provides band ratios of 1.4 (±0.1) for $PhOH^+$–Ar and 2.5 (±0.2) for $PhOH^+$–Kr. Because the relative IR transition intensity (I_{OH}) between ν_{OH}^{π} and ν_{OH}^{H} has been estimated to be ∼2.6 for $PhOH^+$–Ar and ∼3.6 for $PhOH^+$–Kr (Table 1), the relative population ratio evaluated from the static IR spectrum becomes 0.54 (±0.04) for $PhOH^+$–Ar and 0.70 (±0.06) for $PhOH^+$–Kr. These values are in the same order, although those obtained from the picosecond time evolutions (0.59 and 0.94) are somewhat larger than those from the nanosecond IR spectra. These similar results ensure that both analyses are plausible. One possibility for the modest difference from the nanosecond and picosecond results stems from the way to evaluate the intensities. Peak heights are traced from the time evolution, while peak areas are evaluated from the static IR spectra. Relative band intensities from the two methods would give comparable numbers for similar band widths. However, the width of ν_{OH}^{H} is broader and thus the height is suppressed compared with a sharper band with the same peak area. Thus, in the picosecond time evolutions, the relative intensity of the H-bound structure appears somewhat different compared to that of the π-bound structure.

In comparison to the previous report on the dynamics of $PhOH^+$–Kr (τ_+ = ∼20 ps, τ_- = ∼24 ps),[6] the reaction time constants derived in the present study ($\tau_+ = 73$ ps, $\tau_- = 188$ ps) are slower by a factor 3.5–7.8. This large discrepancy probably stems from spectral saturation in the previous study.[6] There, the widths of the bands in the ps-TRIR spectra exceeded 30 cm^{-1} even for ν_{OH}^{π}. This value is more than twice that of the present study, and implies strong saturation in the previous experiment.[6] As a result, the ps-TRIR spectra reached quickly saturated depletion, leading to apparently faster reaction constants. The consistency of the reaction yields from the time-resolved experiments with those derived from the nanosecond IR spectra implies that the ps-TRIR spectra and the time

evolutions in the present experiment observe the true spectral evolution without saturation, yielding the correct dynamics.

3.5 Discussion

The new reaction time constants of $PhOH^+$–Ar and $PhOH^+$–Kr, which are consistent with the static nanosecond spectra provide a reliable qualitative view on the ionization-induced site switching dynamics. It is interesting to note that the site switching in $PhOH^+$–Ar and $PhOH^+$–Kr occurs at roughly the same time scale of $\sim$100 ps. From the theoretical calculations described in Section 3.1, the overall reaction pathways including starting and final points are comparable for both Rg atoms. We may also roughly estimate the forces that drive the Rg atom from the π-site to the H-site. The most convenient parameters would be the intermolecular vibrational frequencies (ν_s, ν_{b1}, ν_{b2}) for the π-bound and H-bound structures. Surprisingly, all three intermolecular frequencies of the π-bound and H-bound minima are comparable for $PhOH^+$–Ar and $PhOH^+$–Kr (Table 1). For example, ν_s, ν_{b1}, and ν_{b2} of $PhOH^+$–Ar(π) are measured as 66, 25, and 15 cm^{-1}, respectively, while those for $PhOH^+$–Kr(π) are determined as 64, 29, and 17 cm^{-1}, respectively.[27,31] This similarity between Rg = Ar and Kr holds also true for the H-bound structures. This means that the force constants for these vibrations in $PhOH^+$–Kr are twice those in $PhOH^+$–Ar, and the factor two in mass of the Rg atom is essentially compensated (m/z 40 and 84 for Ar and Kr). Then, the similar observed time constants for the π → H site switching can be rationalized by classical mechanics because of the similar path length and similar mass-to-force ratio.

Another interesting observation is that at equilibrium (after long delay) the population of the substantially less stable π-bound structure dominates over the more stable H-bound global minimum. The π-bound structure is 1.7 ($PhOH^+$–Ar) or 1.1 times ($PhOH^+$–Kr) more abundant than the H-bound structure. Although the PhOH–Rg dimer is ionized into high vibrational levels above the global minimum, classically the most stable structure should dominate after arriving at the thermodynamic equilibrium. It should be noted that, the quantum chemical calculation suggests that the ν_{OH}^{H} band only reflects structures with H-bonding of the Rg ligand in regions relatively close to the H-bound minimum (within ±2 Å for the case of $PhOH^+$–Kr), because only for those Rg positions the OH stretching frequency will be red-shifted.[1] This may somewhat affect the population ratio of H-bound and π-bound structures derived from the ν_{OH}^{H} and ν_{OH}^{π} intensities in favor of the π isomer (strictly speaking, the signal of the ν_{OH}^{π} band reflects all non H-bonded structures). However, it will not explain the marked difference of the population ratios of $PhOH^+$–Rg to the 100% population of the H-bound structure observed for $PhOH^+$–Ar_2 at long delay.[4,5] Indeed, the lack of bath modes and IVR is essential for the $\pi_1 \leftrightarrow H \leftrightarrow \pi_2$ pendular motion observed in the $PhOH^+$–Rg dimers. In the classical description, the speed of the Rg ligand is fastest at the bottom of the potential curve (H-bound) and zero at the turning point of the pendular motion near the π-bound structure, leading to a population ratio, in which π-bound structures dominate over the more stable H-bound structure.

It is also instructive to consider the quantum mechanical description based on molecular eigenstates and dephasing of wavepackets for the ionization-induced site switching in $PhOH^+$–Rg dimers. As described above, the global minimum of the $PhOH^+$–Rg dimer cation is the H-bound structure, and π-bound structures are local minima although they are the global minima in S_0. Let us assume that the $\pi \leftrightarrow H$ site switching path is an intermolecular vibrational coordinate of a large amplitude motion and focus on this one-dimensional coordinate (Fig. 1). Molecular eigenstates are located above the global H-bound minimum along this coordinate, and eigenstates related to the π-bound structure(s) correspond to higher vibrational levels. Ionization of neutral π-bound PhOH–Rg by picosecond lasers coherently excites a wavepacket composed of several vibrational eigenstates, which corresponds to the initial generation of the π-bound structure in D_0. Subsequently, this wavepacket propagates toward the H-bound global minimum, corresponding to π → H site switching. Since the coupling between the intermolecular reaction coordinate and intramolecular vibrational modes of $PhOH^+$ is weak, the wavepacket simply oscillates within the $\pi_1 \leftrightarrow H \leftrightarrow \pi_2$ triple minimum potential. However, its width is gradually expanding by the dephasing of eigenstates and is finally spread over the whole area between the repulsive potential walls, leading eventually to the $H \leftrightarrow \pi$ equilibrium, which can also be probed by static nanosecond spectroscopy. Hence, the equilibrium populations are determined by the wavefunctions of higher vibrational levels. In case of low vibrational quantum number (or excitation energy), the amplitude of the vibrational wavefunction is larger at the center of the potential curve (H-bound structure). For high excitation, the amplitude becomes large near the repulsive potential walls, corresponding to the π-bound structures, and the equilibrium after dephasing of the wavepacket corresponds to this situation. Therefore, the dominant population of the π-bound structures can also be understood by the dephasing of the wavepacket. The rate of the dephasing directly affects the time evolutions of the π-bound and H-bound structures. It varies with the number and energy spacing of eigenstates which construct the wavepacket. It is thus related to the density of states and not necessarily to the mass of the ligand (Ar, Kr). Thus, a similar time constant for Ar and Kr simply suggests a similar density of states in the initial preparation of the wavepackets. This simple one-dimensional view will not qualitatively change when expanding to the three-dimensional intermolecular case, as the density of states is similar for both Rg atoms (Table 1).

Experimentally, the π → H forward reaction in the $PhOH^+$–Rg dimers ($\tau_+ \sim 100$ ps) is for both Rg atoms (Ar, Kr) roughly one order of magnitude slower than in the $PhOH^+$–Ar_2 trimer ($\tau_+ \sim 7$ ps).[4,5] The picture of dephasing of a wavepacket is also valid for $PhOH^+$–Ar_2. In the global minimum of $PhOH^+$–Ar_2, denoted as $(H10)^+$, one Ar atom is π-bonded and the other one is H-bonded. Photoionization produces a Franck–Condon state, in which both Ar atoms are π-bonded on opposite sites of the

ring, $(11)^+$. The dephasing rate in $PhOH^+$–Ar_2 is faster than in $PhOH^+$–Rg, because of the higher density of states due to the vibrational modes originating from two Ar atoms. It is difficult to predict how much faster the dephasing in $PhOH^+$–Ar_2 is compared to that in $PhOH^+$–Rg. From another viewpoint, in contrast to the $PhOH^+$–Rg dimers, the larger density of intermolecular states arising from the second Rg atom in the $PhOH^+$–Ar_2 trimer can act as bath modes for IVR, which quickly removes energy from the reaction coordinate. As a consequence, the H $\rightarrow$ π back reaction is efficiently quenched in $PhOH^+$–Ar_2, leading to the observation of a single-step $\pi \rightarrow$ H forward reaction with unity yield for the final H-bound $(H10)^+$ reaction product. The reaction mechanism observed for $PhOH^+$–Ar_2 is essentially the same as that for $PhOH^+$–Ar_3,[7] with the major difference of a shorter time constant of $\tau_+ < 3$ ps for the latter cluster due to the larger density of states and shorter isomerization pathway.

4. Summary

ps-TRIR spectroscopy has been applied to $PhOH^+$–Ar and $PhOH^+$–Kr dimers to directly monitor the ionization-induced $\pi \rightarrow$ H site switching reaction. The ps-TRIR spectra show the appearance of ν_{OH}^{π} simultaneously with the photoionization event and the delayed rise of ν_{OH}^{H}. This behavior directly proves that the H-bound structure is generated from the π-bound structure. The coexistence of ν_{OH}^{π} and ν_{OH}^{H} in the ps-TRIR spectra at long delay and in the static nanosecond spectra suggest a $\pi \leftrightarrow$ H equilibrium population induced by the H $\rightarrow$ π back reaction. The classical rate equation analysis based on a modified pendular model reveals time constants of $\tau_+ = 122$ ps and $\tau_- = 155$ ps for $PhOH^+$–Ar and $\tau_+ = 73$ ps and $\tau_- = 188$ ps for $PhOH^+$–Kr. The dispersion-corrected density functional theory calculation at the B3LYP-D3/aug-cc-pVTZ level provides energies and geometries of the π-bound and H-bound minima as well as the connecting transition states. The almost same time constants derived for Ar and the twice heavier Kr atom are rationalized by the classical model based on the comparable potential energy surfaces, reaction pathways, and density of states arising from the similar intermolecular vibrational frequencies obtained from the theoretical calculations. The sharp contrast to the ten times faster single-step one-way $\pi \rightarrow$ H forward reaction in $PhOH^+$–Ar_2 confirms the previous model that the site switching yield strongly depends on the energy dissipation from the reaction coordinate due to IVR.

The ps-TRIR spectra of $PhOH^+$–Ar provide the second example for the $\pi \leftrightarrow$ H equilibrium. This allows us to predict the $\pi \leftrightarrow$ H equilibrium after ionization for other $PhOH^+$–Rg clusters such as Rg = He, Ne, and Xe. Further understanding based on the quantum description requires the precise three-dimensional potential energy surface and solution of the vibrational Schrödinger equation (along with the related wavepacket dynamics), which will hopefully become available in the near future by rapid progress of computer power and computational methods.

Acknowledgements

This work was supported by KAKENHI (JP205104008) on innovative area (2503), KAKENHI (JP16H06028, JP15H02157), and the Cooperative Research Program of the ''Network Joint Research Center for Materials and Devices'' from the Ministry of Education, Culture, Sports, Science and Technology (MEXT), Japan, the Core-to-Core Program 22003 and Bilateral Open Partnership Joint Research Projects from the Japan Society for the Promotion of Science (JSPS), and the Deutsche Forschungsgemeinschaft (DFG, DO 729/4).

References

1 M. Fujii and O. Dopfer, *Int. Rev. Phys. Chem.*, 2012, **31**, 131–173.
2 O. Dopfer and M. Fujii, *Chem. Rev.*, 2016, **116**, 5432–5463.
3 O. Dopfer, *Z. Phys. Chem.*, 2005, **219**, 125–168.
4 S. Ishiuchi, M. Sakai, Y. Tsuchida, A. Takeda, Y. Kawashima, M. Fujii, O. Dopfer and K. Müller-Dethlefs, *Angew. Chem., Int. Ed.*, 2005, **44**, 6149–6151.
5 S. Ishiuchi, M. Sakai, Y. Tsuchida, A. Takeda, Y. Kawashima, O. Dopfer, K. Müller-Dethlefs and M. Fujii, *J. Chem. Phys.*, 2007, **127**, 114307.
6 M. Miyazaki, A. Takeda, S. Ishiuchi, M. Sakai, O. Dopfer and M. Fujii, *Phys. Chem. Chem. Phys.*, 2011, **13**, 2744–2747.
7 S. Ishiuchi, M. Miyazaki, M. Sakai, M. Fujii, M. Schmies and O. Dopfer, *Phys. Chem. Chem. Phys.*, 2011, **13**, 2409–2416.
8 P. Hobza and K. Müller-Dethlefs, *Non-covalent interactions*, The Royal Society of Chemistry, Cambridge, 2010.
9 E. A. Meyer, R. K. Castellano and F. Diederich, *Angew. Chem., Int. Ed.*, 2003, **42**, 1210–1250.
10 L. M. Salonen, M. Ellermann and F. Diederich, *Angew. Chem., Int. Ed.*, 2011, **50**, 4808–4842.
11 B. Brutschy, *Chem. Rev.*, 1992, **92**, 1567–1587.
12 K. S. Kim, P. Tarakeshwar and J. Y. Lee, *Chem. Rev.*, 2000, **100**, 4145–4185.
13 J. C. Ma and D. A. Dougherty, *Chem. Rev.*, 1997, **97**, 1303–1324.
14 A. S. Mahadevi and G. N. Sastry, *Chem. Rev.*, 2013, **113**, 2100–2138.
15 K. Müller-Dethlefs and P. Hobza, *Chem. Rev.*, 2000, **100**, 143–167.
16 D. A. Dougherty, *Science*, 1996, **271**, 163–168.
17 M. S. Cheung, A. E. Garcia and J. N. Onuchic, *Proc. Natl. Acad. Sci. U. S. A.*, 2002, **99**, 685–690.
18 G. A. Papoian, J. Ulander, M. P. Eastwood, Z. Luthey-Schulten and P. G. Wolynes, *Proc. Natl. Acad. Sci. U. S. A.*, 2004, **101**, 3352–3357.
19 R. H. Zhou, *Proc. Natl. Acad. Sci. U. S. A.*, 2003, **100**, 13280–13285.
20 N. Gonohe, H. Abe, N. Mikami and M. Ito, *J. Phys. Chem.*, 1985, **89**, 3642–3648.
21 M. Mons, J. L. Calvé, F. Piuzzi and I. Dimicoli, *J. Chem. Phys.*, 1990, **92**, 2155–2165.

22 A. Fujii, T. Sawamura, S. Tanabe, T. Ebata and N. Mikami, *Chem. Phys. Lett.*, 1994, **225**, 104–107.
23 X. Zhang and J. L. Knee, *Faraday Discuss.*, 1994, **97**, 299–313.
24 O. Dopfer, M. Melf and K. Müller-Dethlefs, *Chem. Phys.*, 1996, **207**, 437–449.
25 C. E. H. Dessent, S. R. Haines and K. Müller-Dethlefs, *Chem. Phys. Lett.*, 1999, **315**, 103–108.
26 C. E. H. Dessent and K. Müller-Dethlefs, *Chem. Rev.*, 2000, **100**, 3999–4022.
27 S. R. Haines, C. E. H. Desent and K. Müller-Dethlefs, *J. Electron Spectrosc. Relat. Phenom.*, 2000, **108**, 1–11.
28 N. Solcà and O. Dopfer, *Chem. Phys. Lett.*, 2000, **325**, 354–359.
29 N. Solcà and O. Dopfer, *J. Mol. Struct.*, 2001, **563–564**, 241–244.
30 N. Solcà and O. Dopfer, *J. Phys. Chem. A*, 2001, **105**, 5637–5645.
31 S. Ullrich, G. Tarczay and K. Müller-Dethlefs, *J. Phys. Chem. A*, 2002, **106**, 1496–1503.
32 N. Solcà and O. Dopfer, *Chem. Phys. Lett.*, 2003, **369**, 68–74.
33 S. Ishiuchi, Y. Tsuchida, O. Dopfer, K. Müller-Dethlefs and M. Fujii, *J. Phys. Chem. A*, 2007, **111**, 7569–7575.
34 A. Takeda, H.-S. Andrei, M. Miyazaki, S. Ishiuchi, M. Sakai, M. Fujii and O. Dopfer, *Chem. Phys. Lett.*, 2007, **443**, 227–231.
35 I. Kalkman, C. Brand, T.-B. C. Vu, W. L. Meerts, Y. N. Svartsov, O. Dopfer, K. Müller-Dethlefs, S. Grimme and M. Schmitt, *J. Chem. Phys.*, 2009, **130**, 224303.
36 A. Armentano, M. Riese, M. Taherkahani, M. B. Yezzar, K. Müller-Dethlefs, M. Fujii and O. Dopfer, *J. Phys. Chem. A*, 2010, **114**, 11139–11143.
37 X. Tong, A. Armentano, M. Riese, M. B. Yezzar, S. M. Pimblott, K. Müller-Dethlefs, S. Ishiuchi, M. Sakai, A. Takeda, M. Fujii and O. Dopfer, *J. Chem. Phys.*, 2010, **133**, 154308.
38 A. Armentano, X. Tong, M. Riese, S. M. Pimblott, K. Müller-Dethlefs, M. Fujii and O. Dopfer, *Phys. Chem. Chem. Phys.*, 2011, **13**, 6071–6076.
39 M. Miyazaki, S. Tanaka, S. Ishiuchi, O. Dopfer and M. Fujii, *Chem. Phys. Lett.*, 2011, **513**, 208–211.
40 M. Schmies, A. Patzer, M. Fujii and O. Dopfer, *Phys. Chem. Chem. Phys.*, 2011, **13**, 13926–13941.
41 M. Miyazaki, S. Yoshikawa, F. Michels, K. Misawa, S. Ishiuchi, M. Sakai, O. Dopfer, K. Müller-Dethlefs and M. Fujii, *Phys. Chem. Chem. Phys.*, 2015, **17**, 2494–2503.
42 J. Makarewicz, *J. Chem. Phys.*, 2006, **124**, 084310.
43 J. Černý, X. Tong, P. Hobza and K. Müller-Dethlefs, *Phys. Chem. Chem. Phys.*, 2008, **10**, 2780–2784.
44 J. Černý, X. Tong, P. Hobza and K. Müller-Dethlefs, *J. Chem. Phys.*, 2008, **128**, 114319.
45 M. Miyazaki, A. Takeda, M. Schmies, M. Sakai, K. Misawa, S. Ishiuchi, F. Michels, K. Müller-Dethlefs, O. Dopfer and M. Fujii, *Phys. Chem. Chem. Phys.*, 2014, **16**, 110–116.
46 O. Dopfer, G. Reiser, K. Müller-Dethlefs, E. W. Schlag and S. D. Colson, *J. Chem. Phys.*, 1994, **101**, 974–989.
47 K. Tanabe, M. Miyazaki, M. Schmies, A. Patzer, M. Schütz, H. Sekiya, M. Sakai, O. Dopfer and M. Fujii, *Angew. Chem., Int. Ed.*, 2012, **51**, 6604–6607.
48 K. Sakota, S. Harada, Y. Shimazaki and H. Sekiya, *J. Phys. Chem. A*, 2011, **115**, 626–630.
49 T. Nakamura, M. Schmies, A. Patzer, M. Miyazaki, S. Ishiuchi, M. Weiler, O. Dopfer and M. Fujii, *Chem. – Eur. J.*, 2014, **20**, 2031–2039.
50 T. Nakamura, M. Miyazaki, S. Ishiuchi, M. Weiler, M. Schmies, O. Dopfer and M. Fujii, *ChemPhysChem*, 2013, **14**, 741–745.
51 M. Wohlgemuth, M. Miyazaki, M. Weiler, M. Sakai, O. Dopfer, M. Fujii and R. Mitrić, *Angew. Chem., Int. Ed.*, 2014, **53**, 14601–14604.
52 M. J. Frisch, G. W. Trucks, H. B. Schlegel, G. E. Scuseria, M. A. Robb, J. R. Cheeseman, G. Scalmani, V. Barone, B. Mennucci, G. A. Petersson, H. Nakatsuji, M. Caricato, X. Li, H. P. Hratchian, A. F. Izmaylov, J. Bloino, G. Zheng, J. L. Sonnenberg, M. Hada, M. Ehara, K. Toyota, R. Fukuda, J. Hasegawa, M. Ishida, T. Nakajima, Y. Honda, O. Kitao, H. Nakai, T. Vreven, J. J. A. Montgomery, J. E. Peralta, F. Ogliaro, M. Bearpark, J. J. Heyd, E. Brothers, K. N. Kudin, V. N. Staroverov, T. Keith, R. Kobayashi, J. Normand, K. Raghavachari, A. Rendell, J. C. Burant, S. S. Iyengar, J. Tomasi, M. Cossi, N. Rega, J. M. Millam, M. Klene, J. E. Knox, J. B. Cross, V. Bakken, C. Adamo, J. Jaramillo, R. Gomperts, R. E. Stratmann, O. Yazyev, A. J. Austin, R. Cammi, C. Pomelli, J. W. Ochterski, R. L. Martin, K. Morokuma, V. G. Zakrzewski, G. A. Voth, P. Salvador, J. J. Dannenberg, S. Dapprich, A. D. Daniels, O. Farkas, J. B. Foresman, J. V. Ortiz, J. Cioslowski and D. J. Fox, *Gaussian 09, Gaussian, Inc., Revision D.01*, Wallingford, CT, 2013.
53 A. Fujii, A. Iwasaki, T. Ebata and N. Mikami, *J. Phys. Chem. A*, 1997, **101**, 5963–5965.
54 C. Ratzer, J. Küpper, D. Spangenberg and M. Schmitt, *Chem. Phys.*, 2002, **283**, 153–169.

